Nano-Micro Letters

e-ISSN 2150-5551
CN 31-2103/TB

ARTICLE

https://doi.org/10.1007/s40820-026-02319-0

Cite as
Nano-Micro Lett.
(2027) 19:26

Received: 1 April 2026
Accepted: 8 July 2026

Bioinspired Molecular Magnetic Field-Responsive Catalyst for On-Demand Switching of 2e⁻ and 4e⁻ Oxygen Reduction

Boying Zhang[1], Qiaoling Guo[1], Haochuan Li[1], Yue Wang[1], Qing Li[1], Haining Liu[1,2] ✉, Shanlin Qiao[1,2,3] ✉

HIGHLIGHTS

- The bioinspired molecular magnetic field responsive catalysts were synthesized to selectively switch between the 2e⁻ and 4e⁻ oxygen reduction reaction (ORR) pathways.
- The molecular magnetic field responsive catalyst integrated with single domain Fe_3O_4 delivers a significantly boosted H_2O_2 selectivity of 63.9% (electron transfer number, $n = 2.72$), whereas the multi domain Fe_3O_4 incorporated variant effectively redirects the ORR exclusively toward the 4e⁻ pathw ay ($n = 3.67$).

ABSTRACT Achieving precise and on-demand steering of the oxygen reduction reaction (ORR) pathway between the efficient 4e⁻ route to H_2O and the valuable 2e⁻ route to H_2O_2 remains a pivotal challenge in electrocatalysis. Herein, we address this challenge by designing a bioinspired molecular magnetic field-responsive catalyst (MMFR-C) via magnetic single-atom-anchored Salen-based covalent organic frameworks (MSA-Salen COFs) onto magnetic nanoparticles (single/multi-domain Fe_3O_4). Mimicking cytochrome *c* oxidase, the MMFR-C employs MSA-Salen COFs as an ordered proton-transfer channel and well-defined N_2-M-O_2 moieties as enzymatic O_2 activation sites, with Fe_3O_4 providing a built-in magnetic field for remote regulation of the active-site electronic structure. The bioinspired MMFR-C exhibits switchable ORR pathways. Relative to the pristine Co-Salen COF (26% H_2O_2 selectivity, $n=3.48$), the MMFR-C integrated with a single-domain Fe_3O_4 exhibits a remarkably enhanced H_2O_2 selectivity of 63.9% ($n=2.72$), while that with a multi-domain Fe_3O_4 diverts the ORR pathway toward the 4e⁻ route ($n=3.67$). (i) We elucidate that the uniform magnetic field from the single-domain Fe_3O_4 in MMFR-C favors orbital hybridization between its active N_2-M-O_2 moieties and the *OOH intermediate, with moderate *OOH adsorption suppressing O–O scission and thus steering ORR selectivity toward H_2O_2. (ii) In contrast, the enhanced specific magnetism from its multi-domain Fe_3O_4 core optimizes the *d*-band center of MMFR-C's active sites, stabilizes triplet O_2 adsorption, and reduces spin-forbidden transition barriers, thereby facilitating O–O cleavage and diverting its ORR pathway to the 4e⁻ route.

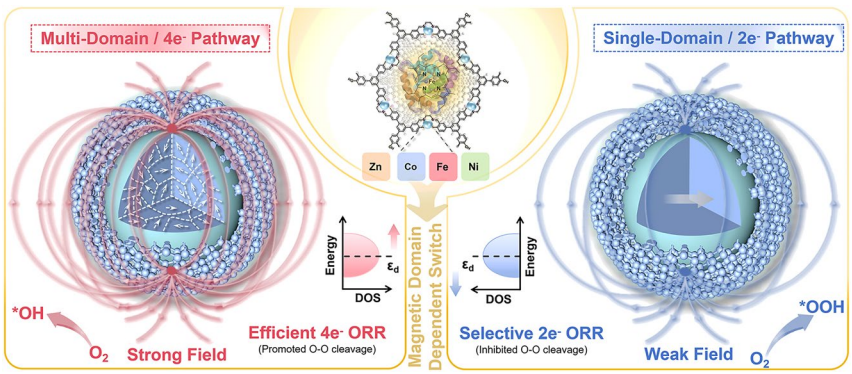

KEYWORDS Molecular magnetic field-responsive catalyst; Metal-Salen covalent organic frameworks; Oxygen reduction reaction; Selectivity regulation

Boyingzhang and Qiaoling Guo contributed equally to this work.

✉ Haining Liu, liuhn@hebust.edu.cn; Shanlin Qiao, ccpeslqiao@hebust.edu.cn
[1] College of Chemistry and Pharmaceutical Engineering, Hebei University of Science and Technology, Shijiazhuang 050018, People's Republic of China
[2] Hebei Research Center of Pharmaceutical and Chemical Engineering, Shijiazhuang 050018, People's Republic of China
[3] Hebei Engineering Research Center of Organic Solid Photoelectric Materials for Electronic Information, Shijiazhuang 050018, People's Republic of China

Published online: 10 August 2026

1 Introduction

The highly efficient oxygen reduction reaction (ORR) is found in nature, which plays a pivotal role in biological respiration and electrochemical energy conversion [1, 2]. However, achieving precise and on-demand steering of the ORR pathway between the efficient $4e^-$ ORR pathway to H_2O and the valuable $2e^-$ ORR to H_2O_2 remains a pivotal challenge [3–6]. This difficulty originates from the complex multi-electron/proton-coupled kinetics of ORR, where the critical bifurcation is dictated by whether the oxygen–oxygen (O–O) bond cleaves [7–9]. Over the past years, strategies for controlling O–O bond cleavage strategies, including metal atom doping [10–13], heterojunction engineering [14, 15], and coordination environment optimization [16–19], have primarily relied on structural modifications of the active sites. However, such approaches inherently require alteration of the catalyst structure. In contrast, applying an external magnetic field provides a non-invasive and sustainable means to tune both activity and selectivity in real time, without altering the catalyst itself [20–22]. A recent study demonstrates the application of the magnetic modulation of the *eg*-orbital occupancy of Co ions to boost the two-electron oxygen reduction electrocatalysis for faster water decontamination [23]. Moreover, the built-in magnetic field can transfer the Co center from a low-spin (LS) state to a high-spin (HS) state without changing the atomic structure, thereby increasing the turnover frequency by an order of magnitude, enhancing the H_2O_2 selectivity of the ORR by 50% [24]. Prior efforts have mainly focused on magnetic field-enhanced electrocatalytic activity, yet the rational switching of ORR selectivity on the foundation of improved activity remains highly desirable and largely underexplored.

In nature, cytochrome *c* oxidase (CcO) catalyzes the reduction of oxygen to water, an essential reaction in cellular respiration [25]. In CcO, O_2 binding and activation occur at the heme/Cu binuclear center. In the fully reduced state, the Cu^+ species donates electrons to the adsorbed O_2, facilitating the formation of the key Fe^{3+}-peroxo-Cu^{2+} intermediate and subsequent cleavage of the O–O bond. This electron-donating effect provides the essential thermodynamic driving force for the complete $4e^-$ ORR pathway, leading to the exclusive production of H_2O [26–28]. If the Cu center is locked in the Cu^{2+} state and loses its electron-donating capability, the electron density at the active site becomes insufficient to drive O–O bond scission. The peroxo intermediate thus remains stable with an intact O–O moiety, forcing the reaction to shift toward the $2e^-$ ORR pathway that generates H_2O_2 instead. Inspired by the dynamic electron-donating modulation via Cu valence evolution in CcO, where reversible electron transfer dictates ORR pathway selectivity. Molecular magnetic field can dynamically tune the electronic configuration, spin state, and electron-donating capability of metal sites. We reason that a molecular magnetic field could serve as a non-invasive and controllable tool to mimic this biological electron-regulating behavior in artificial catalytic systems. On this basis, we put forward the concept of constructing a bioinspired molecular magnetic field-responsive catalyst (MMFR-C), intended to regulate the electron-donation behavior of active metal sites and thereby achieve programmable switching between the $2e^-$ and $4e^-$ ORR pathways.

Herein, we materialize this concept by fabricating a class of bioinspired MMFR-C, achieved by anchoring magnetic single atoms in Salen-based covalent organic frameworks (Salen COFs) (Metal = Zn, Fe, Co, Ni) that parcel magnetic Fe_3O_4 nanoparticles (Scheme 1). As a cytochrome *c* oxidase mimic, MMFR-C integrates ordered proton-transfer channels from magnetic single-atom-anchored (MSA)-Salen COFs and well-defined N_2-M-O_2 moieties as efficient O_2 activation sites, while the embedded Fe_3O_4 component generates a built-in magnetic field that remotely modulates the electronic structure of the active sites. Notably, the bioinspired MMFR-C enables controllable switching between ORR pathways simply by varying the magnetic domain structure of Fe_3O_4. Specifically, MMFR-C incorporating single-domain Fe_3O_4 delivers high H_2O_2 selectivity (63.9%, $n = 2.72$), whereas the counterpart with multi-domain Fe_3O_4 redirects the reaction toward the $4e^-$ pathway ($n = 3.67$), both exhibiting superior tunability relative to the pristine Co-Salen COF (H_2O_2 selectivity = 26%, $n = 3.48$). It is further confirmed that the weak, uniform magnetic field in single-domain Fe_3O_4 gives rise to moderate *OOH adsorption that inhibits O–O cleavage, favoring the $2e^-$ ORR toward H_2O_2. By contrast, the stronger intrinsic field in multi-domain Fe_3O_4 optimizes the *d*-band center and lowers spin-transition barriers, facilitating O–O cleavage and promoting the $4e^-$ route.

https://doi.org/10.1007/s40820-026-02319-0

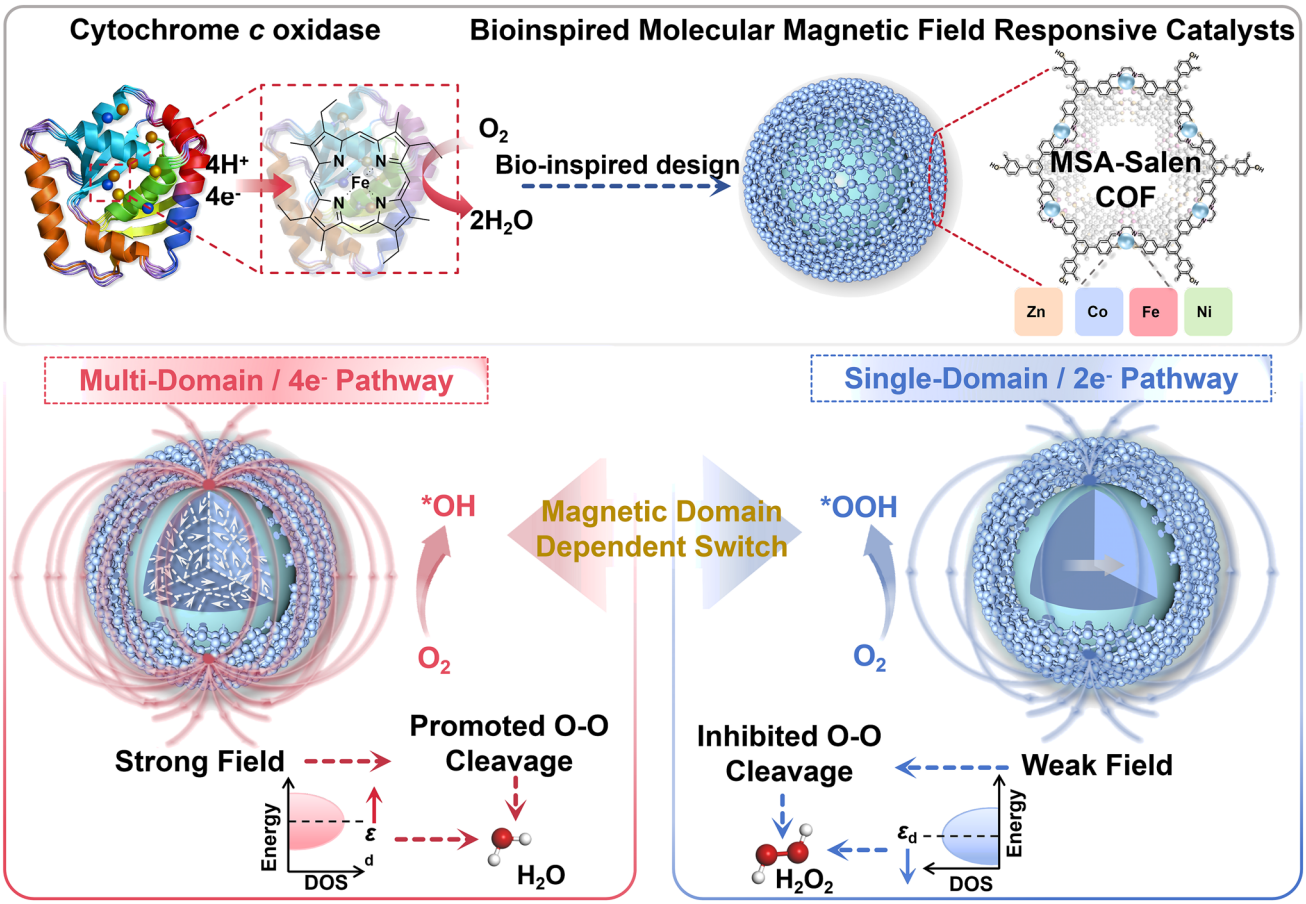

Scheme 1 Schematic diagram of the design and catalytic mechanism of the MMFR-C catalyst

2 Experimental

2.1 Materials

Reagents and solvents, readily available commercially, were utilized without additional purification. Detailed information is available in the Supporting Information.

2.2 Synthesis of Zn-Salen COF

1,3,5-tris(4′-hydroxy-5′-formylphenyl)benzene (THB) (0.03 mmol, 13.2 mg) and $Zn(OAC)_2{\cdot}2H_2O$ (14.8 mg) were weighed into a Pyrex tube (volume of ca. 10 mL). The mixture was dissolved in 1.5 mL of mesitylene/ethanol (1:1 v/v) and sonicated for 5 min. Then, ethanediamine (0.045 mmol, 5 µL) was added to the mixture. The mixed solution was ultrasonicated for another 2 min. After the aqueous acetic acid (6 M, 0.15 mL) was added, the solution was sonicated for 5 min to ensure uniform dispersion. The Pyrex tube was degassed through three freeze–pump–thaw cycles and then flame-sealed. The tube was placed in an oven at 120 °C for 3 days. When the reaction time was up, the ampoule was cooled to room temperature and opened. The product was collected by centrifugation and then cleaned with N, N-dimethylformamide (DMF), ethanol, and acetone. The powder was dried in an oven at 100 °C under vacuum overnight.

2.3 Synthesis of MSA-Salen COFs

The Zn-Salen COF and $M(OAc)_2{\cdot}nH_2O$ were weighed into a glass vial, and dry ethyl alcohol was added. The mixture was continuously stirred at room temperature for 48 h, with the solution being refreshed three times. The solid was collected by centrifugation and washed with ethyl alcohol and

acetone several times. The powder was dried in an oven at 80 °C under vacuum overnight (Metal: Fe, Co, Ni).

2.4 Synthesis of s-Fe_3O_4@Zn-Salen COF

Weigh single-domain nanoparticles s-Fe_3O_4 (4.6 mg) and add it to approximately 10 mL of a Pyrex tube, then add a mesitylene/ethanol (1.5 mL, 1:1 v/v) solution and ultrasonically treat for 10 min to disperse the Fe_3O_4 homogeneously. Next, add ethylenediamine (0.045 mmol, 5 μL) and sonicate for 5 min. Subsequently, weigh THB (0.03 mmol, 13.2 mg) and $Zn(OAc)_2{\cdot}2H_2O$ (14.8 mg) and add them to the mixed solution, followed by ultrasonic treatment for 10 min. After adding aqueous acetic acid (6 M, 0.15 mL), continue ultrasonic treatment for 5 min to ensure uniform dispersion. Degas the Pyrex tube via three freeze–pump–thaw cycles and seal it by flame. Place the tube in an oven at 120 °C and dry for 3 days. At the end of the reaction, cool the ampoule to room temperature and open it. Collect the product by centrifugation and wash with DMF, ethanol, and acetone. Dry the powder overnight in a vacuum oven at 100 °C to obtain s-Fe_3O_4@Zn-Salen-COF (20 wt% Fe_3O_4) composites of various sizes.

2.5 Synthesis of m-Fe_3O_4@Zn-Salen COFs

The composite m-Fe_3O_4@Zn-Salen COF (20 wt% Fe_3O_4) was prepared using a procedure identical to that described for s-Fe_3O_4@Zn-Salen COF, except that multi-domain Fe_3O_4 nanoparticles (m-Fe_3O_4, ≈150 nm) were used in place of the single-domain nanoparticles (s-Fe_3O_4, ≈10 nm). All other reactants, solvents, and reaction conditions remained the same.

2.6 Synthesis of s/m-Fe_3O_4@MSA-Salen COFs

The s/m-Fe_3O_4@Zn-Salen COFs and $M(OAc)_2{\cdot}nH_2O$ were weighed into a glass vial, and dry ethyl alcohol was added. The mixture was continuously stirred at room temperature for 48 h, with the solution being refreshed three times. The solid was collected by centrifugation and washed with ethyl alcohol and acetone several times. The powder was dried in an oven at 80 °C under vacuum overnight (Metal: Fe, Co, Ni).

2.7 Electrochemical Performance Tests

Electrochemical measurements were performed using a rotating ring-disk electrode (RRDE) system integrated with a CHI 760E electrochemical workstation. A glassy carbon disk/platinum ring RRDE electrode (Ø = 5.61 mm) from PINE was used as the work electrode. A graphite rod and an Ag/AgCl electrode were used as the counter and reference electrodes, respectively. All potentials were converted to the reversible hydrogen electrode (RHE) scale using the Nernst equation (Eq. 1).

$$E_{RHE} = E_{Ag/AgCl} + 0.197 + 0.0591 \times pH \quad (1)$$

Each catalyst sample (5 mg) was dispersed in 1 mL of a mixed solution comprising ethanol, deionized water, and Nafion solution (5 wt%) in a volume ratio of 9:10:1 (v/v/v). The resulting suspension was sonicated for 30 min to ensure homogeneous dispersion. 10 μL of ink was loaded onto the RRDE electrode and dried at 500 rpm. Before testing, the electrolyte was saturated with oxygen by continuously passing oxygen through the 0.1 M KOH electrolyte for 30 min. Subsequently, a 30-cycle cyclic voltammetry (CV) sweep (sweep rate 50 mV s^{-1}) was performed to activate the catalyst, with the oxygen continuously applied during the test. The catalyst was stabilized when the CV curve remained essentially unchanged. After the CV activation was completed, the test was suspended again, and oxygen was added for 20 min to replenish the dissolved oxygen consumed during the CV test, and then, the LSV test was performed. A linear voltage of 0.2−0.8 V vs. Ag/AgCl was applied to the disk electrode, and 1.3 V vs. RHE was applied to the ring electrode, with a scan rate of 10 mV s^{-1} and a RRDE rotation speed at 400−1600 rpm. After 30 min of continuous nitrogen in the electrolyte, a CV scan was performed to test the background current in this system to verify that the reaction occurring in the system was an oxygen reduction reaction.

3 Results and Discussion

3.1 Synthesis and Characterization

The bioinspired MMFR-C (s-Fe_3O_4@Zn-Salen COF and m-Fe_3O_4@Zn-Salen COF) was synthesized according to an in situ growth strategy, using THB, $Zn(OAC)_2{\cdot}2H_2O$,

https://doi.org/10.1007/s40820-026-02319-0

and ethane diamine in the presence of single-/multi-domain Fe_3O_4 with mesitylene and ethanol as the solvent, as well as acetic acid aqueous solution as the catalyst. Zn-Salen COF can be synthesized under the above conditions in the absence of Fe_3O_4 according to the previous method [29]. The framework features readily accessible 1D channel arrays and dynamic N_2-Zn-O_2 coordination bonds, which facilitate metal ion exchange [30]. Therefore, the as-synthesized Zn-Salen COF, s-Fe_3O_4@Zn-Salen COF, and m-Fe_3O_4@Zn-Salen COF were immersed in saturated aqueous solutions of metal acetate salts, including $Co(OAc)_2{\cdot}2H_2O$, $Fe(OAc)_2{\cdot}H_2O$, and $Ni(OAc)_2{\cdot}4H_2O$ for 2 days. Inductively coupled plasma optical emission spectrometry (ICP-OES) was used to analyze the metal content for Ni-Salen COF, Co-Salen COF, and Fe-Salen COF (Table S1). The Ni, Co, and Fe contents in the Ni-Salen COF, Co-Salen COF, and Fe-Salen COF are 5.48, 5.65, and 5.22 wt%, respectively.

Fourier transform infrared spectroscopy (FT-IR) spectra of THB, MSA-Salen COF, and MMFR-C (Fig. S2) reveal the disappearance of the characteristic C=O stretching vibration at 1655 cm^{-1}, while peaks corresponding to C=N bonds emerge at 1630 and 1134 cm^{-1}. This confirms the successful polycondensation between THB and ethane diamine. As shown in Fig. 1a, the powder X-ray diffraction (PXRD) patterns of Zn-Salen COF, s-Fe_3O_4@Zn-Salen COF, and m-Fe_3O_4@Zn-Salen COF exhibit strong diffraction peaks at 3.54°, 7.12°, 9.36°, and 12.32°, which correspond to the (100), (200), (210), and (220) facets, respectively. It is confirmed that the crystalline structure of the Zn-Salen COF is retained after the preparation of the MMFR-C.

These experimental diffraction features are consistent with the simulated pattern based on an AA-stacking model. Furthermore, the PXRD pattern of s/m-Fe_3O_4@MSA COF displays characteristic peaks at 30.3°, 35.7°, and 43.2°, which are indexed to the (220), (311), and (400) facets of Fe_3O_4 (JCPDS card no. 99–0073). As shown in Fig. S3a–c, PXRD revealed that the MSA-Salen COF and MMFR-C retained the original crystal structure and high crystallinity after ion exchange.

The porosity of MSA-Salen COF and s/m-Fe_3O_4@Zn-Salen COF was studied by nitrogen sorption measurement at 77 K. As shown in Fig. S4a, b, the Zn-Salen COF and s/m-Fe_3O_4@Zn-Salen COF isotherms are type-IV isotherms with the characteristics of mesoporous, as indicated by the International Union of Pure and Applied Chemistry. The BET surface areas of Zn-Salen COF, s-Fe_3O_4@Zn-Salen COF, and m-Fe_3O_4@Zn-Salen COF were calculated to be 1456, 1242, and 1191 $m^2\ g^{-1}$ (Fig. 1b). Pore size distribution was calculated by means of quenched solid density functional theory (QS-DFT). Notably, Zn-Salen COF, s-Fe_3O_4@Zn-Salen COF, and m-Fe_3O_4@Zn-Salen COF share comparable pore sizes of 2.5 nm, suggesting that the introduction of Fe_3O_4 nanoparticles does not alter the intrinsic pore structure of the Zn-Salen COF matrix (Figs. 1b and S4b).

Transmission electron microscopy (TEM) confirms the successful fabrication of MMFR-C. Spherical single-domain (s-Fe_3O_4, ~ 10 nm) and multi-domain (m-Fe_3O_4, ~ 150 nm) nanoparticles were employed (Figs. S5 and S6), and both are fully encapsulated by porous shells. High-resolution TEM (HRTEM) identifies a well-ordered 2.3 nm lattice fringe in the porous shell, which can be indexed to the (100) facet of Zn-Salen COF, and a 0.29 nm lattice fringe characteristic of the (220) facet of spinel Fe_3O_4. Additionally, HRTEM confirms that metal-exchanged MMFR-C maintain well-defined morphologies and high crystallinity (Fig. S7a–c).

To further investigate the local electronic environment and coordination geometry of Zn-Salen COF, X-ray absorption near-edge structure (XANES) and extended X-ray absorption fine structure (EXAFS) measurements were conducted at the Zn K-edge. Zn K-edge XANES spectra of Zn-foil, ZnO, and Zn-Salen COF (Fig. 1c) confirm that Zn atoms in Zn-Salen COF are cationic, as their adsorption edges are higher than that of Zn foil. The Fourier-transformed EXAFS spectrum of Zn-Salen COF (Fig. 1d) shows a single peak at 1.51 Å, assigned to the Zn–O/N scattering path [31], and the absence of a Zn−Zn bond at ~ 2.2 Å indicates atomic dispersion of Zn. Fitting results of EXAFS in *R*, *k*, and *q* space (Figs. 1e and S8, Table S2) further confirm Zn atoms in Zn-Salen COF adopt an N_2-Zn-O_2 coordination mode with two N and two O atoms, verifying the formation of a Zn–O/N coordination structure. Additionally, wavelet transform (WT) analysis (Fig. 1f) provides atomic-level resolution of metal distribution, with a single intensity maximum at ~ 5.0 $Å^{-1}$ directly evidencing atomic dispersion of Zn ions in the N_2-O_2 chelating pockets of Salen ligands, forming well-defined N_2-Zn-O_2 single sites [32].

X-ray photoelectron spectroscopy (XPS) was used to determine the surface element concentration and chemical state. XPS spectra confirm the presence of C, N, O, and corresponding metal ions in both MSA-Salen COFs and s/m-Fe_3O_4@MSA-Salen COF, further verifying the successful incorporation of Ni, Co, and Fe atoms into Zn-Salen COF

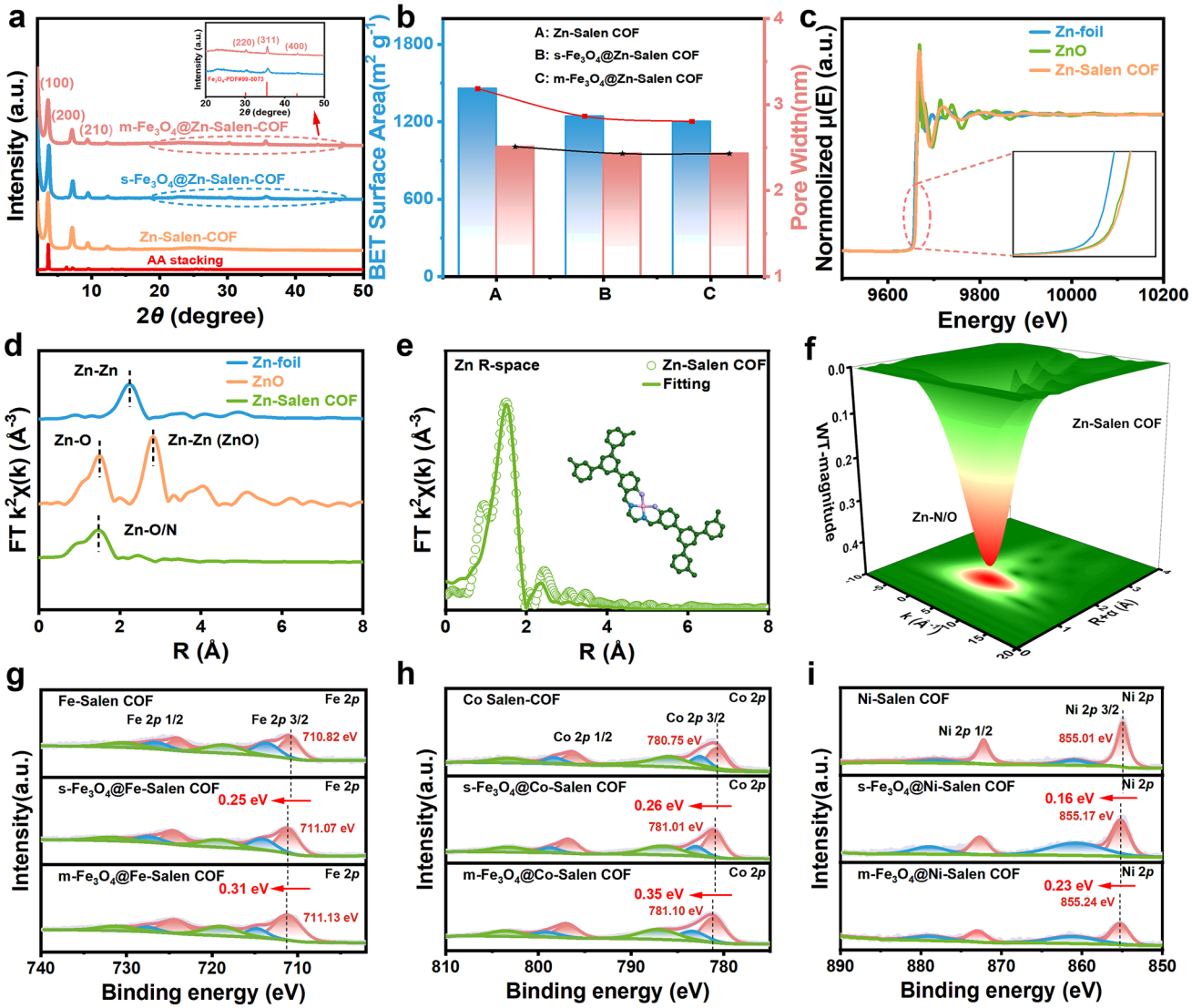

Fig. 1 **a** PXRD pattern and **b** Brunauer–Emmett–Teller (BET) surface area, and total pore volume of Zn-Salen-COF and s/m-Fe_3O_4@Zn-Salen-COF, **c** Zn K-edge XANES spectra for Zn-foil, ZnO, and Zn-Salen-COF. **d** Fitting result of the EXAFS spectra of Zn-Salen COF at R space. **e** Corresponding k^2-weight Fourier transforms of the Zn K-edge EXAFS spectra. **f** WT of the Zn *k*-edge of 3*d* for Zn-Salen COF. High-resolution XPS spectra of **g** Ni 2*p*, **h** Co 2*p*, and **i** Fe 2*p* of MSA-Salen COFs and s-Fe_3O_4@MSA-Salen COFs, respectively

and s/m-Fe_3O_4@Zn-Salen COF structures. Notably, residual Zn^{2+} remains in Ni-Salen, Co-Salen, and Fe-Salen COF after ion exchange, attributed to the kinetic equilibrium of coordination bonds. High-resolution N 1*s* and O 1*s* XPS spectra of MSA-Salen COFs and MMFR-C are displayed in Figs. S9–S10. The deconvoluted N 1 *s* spectra present two dominant peaks at 399.5 ± 0.2 and 400.5 ± 0.3 eV, corresponding to Metal–N and C=N bonds, respectively (Fig. S9). Similarly, the deconvoluted O 1 *s* spectra show two peaks at 531.8 ± 0.6 and 532.5 ± 0.5 eV, assigned to O–Metal and C–O species, respectively (Fig. S10). This confirms that metal centers are anchored in N_2-O_2 ligands, consistent with EXAFS results. The slightly higher O–Metal content in MMFR-C than in pristine MSA-Salen COFs due to combined Fe–O (from Fe_3O_4) and O–Metal (from COFs) verifies Fe_3O_4 incorporation in the composites.

As shown in Figs. 1g–i and S11, the Ni 2*p*, Co 2*p*, and Fe 2*p* peaks in s/m-Fe_3O_4@Ni-Salen COF, s/m-Fe_3O_4@Co-Salen COF, and s/m-Fe_3O_4@Fe-Salen COF shift to higher binding energies by 0.16/0.23, 0.26/0.35, and 0.25/0.31 eV, respectively. The positive binding energy shift indicates a reduced local electron density around Ni, Co, and

https://doi.org/10.1007/s40820-026-02319-0

Fe centers, which originates from strong electronic interactions with Fe_3O_4 within the MMFR-C. Notably, m-Fe_3O_4 induces a larger positive shift than s-Fe_3O_4. This trend arises from the stronger intrinsic magnetic field of multi-domain Fe_3O_4, which amplifies interfacial electronic interactions in the bioinspired MMFR-C and enhances electron withdrawal from the metal sites. Notably, the shift magnitude exhibits a strong metal-dependent behavior. The Zn 2*p* signal in s/m-Fe_3O_4@Zn-Salen COF shows negligible binding energy variation, owing to the stable d^{10} configuration, non-magnetic nature, and weak electron-donating character of Zn^{2+}, which lead to minimal electronic coupling with Fe_3O_4 [33]. In sharp contrast, distinct positive shifts are observed for magnetic metal centers (Ni, Co, Fe). The shift increases in the order Ni < Co≈Fe, consistent with the increasing number of unpaired *d* electrons and thus the stronger intrinsic magnetic moment of the metal center. These results demonstrate that the magnetic moment of the active metal site and the magnetic domain size of Fe_3O_4 act in synergy to modulate interfacial electron transfer within MMFR-C. The gradient electronic regulation induced by different Fe_3O_4 domains directly tailors the electron density of active metal centers, which further dictates the selective switching between $2e^-$ and $4e^-$ ORR pathways.

3.2 Magnetic Characterization

To further elucidate the electronic structures of MSA-Salen COFs and MMFR-C, magnetic hysteresis loops were measured at room temperature. MSA-Salen COFs show linear, reversible, and monotonic magnetic responses, consistent with their intrinsic paramagnetic character (Fig. S12a) [34]. The calculated magnetic susceptibilities (χ) for Zn-, Ni-, Co-, and Fe-Salen COF are 7.766×10^{-7}, 8.362×10^{-7}, 1.453×10^{-6}, and 1.047×10^{-6}, respectively. Notably, clear magnetic domain behaviors are distinguished in MMFR-C (Fig. 2a), the 10 nm Fe_3O_4-based composite shows negligible hysteresis, characteristic of single-domain behavior, whereas the 150 nm sample exhibits obvious hysteresis, typical of multi-domain behavior [35, 36]. Accordingly, m-Fe_3O_4@MSA-Salen COFs display significantly higher saturation magnetization (*Ms*) than s-Fe_3O_4@MSA-Salen COFs, confirming a strong correlation between magnetic domain structure and saturation magnetization (Figs. 2b and S12b, c). These results demonstrate that the Fe_3O_4 cores not only endow the MMFR-C with tunable magnetic properties but also serve as built-in molecular magnetic field regulators to modulate the electronic structure of metal centers.

Zero-field cooling (ZFC) variable-temperature magnetization measurements further suggest that MSA-Salen COFs are paramagnetic (Fig. S13). As shown in Figs. 2c and S13a, b, the magnetic susceptibilities (χ_m) of MMFR-C are significantly higher than those of their MSA-Salen COF counterparts. According to the Curie–Weiss law [$\chi_m = C/(T-\theta)$, where C is the Curie constant, and θ is the Curie temperature] [37], the effective magnetic moment (μ_{eff}) can be derived from the relation $\mu_{eff} = (8C)^{1/2}$ and is further correlated with the number of unpaired electrons (n) via $\mu_{eff} = [n(n+2)]^{1/2}$. The calculated μ_{eff} for s-Fe_3O_4@Zn-Salen COF, s-Fe_3O_4@Co-Salen COF, s-Fe_3O_4@Fe-Salen COF, and s-Fe_3O_4@Ni-Salen COF are 5.11, 6.93, 7.04, and 6.52 μ_B, respectively, all significantly higher than those of the corresponding pristine Zn-Salen COF (0.097 μ_B), Co-Salen COF (0.37 μ_B), Fe-Salen COF 0.216 μ_B), and Ni-Salen COF (0.123 μ_B). A higher μ_{eff} reflects a larger effective magnetic moment and increased unpaired electron [38]. The enhanced μ_{eff} in s-Fe_3O_4@MSA-Salen COFs further validates that MMFR-C can efficiently modulate the spin state of active metal centers, with the magnetic Fe_3O_4 core serving as a built-in field source that exerts a more significant effect on metals with stronger intrinsic magnetism. These results demonstrate that the bioinspired MMFR-C enables controllable spin polarization of single-atom sites via internal magnetic field regulation, laying the structural foundation for switchable ORR pathways.

Electron spin resonance (ESR) spectra reveal a distinct resonance signal for MSA-Salen COFs (Fig. S14), indicative of unpaired electrons inherent to these frameworks. Relative to pristine MSA-Salen COFs, the s-Fe_3O_4@MSA-Salen COF composites in the bioinspired MMFR-C series exhibit a markedly enhanced ESR response (Fig. 2d). This intensified signal signifies an increased population of unpaired electrons, confirming that the Fe_3O_4-derived built-in magnetic field within MMFR-C effectively modulates the electronic structure of atomic metal sites [39]. Quantitative ESR analysis yields spin concentrations of 0, 1.81×10^{14}, 2.24×10^{16}, and 2.52×10^{16} spin g^{-1} for s-Fe_3O_4@Zn-, Ni-, Co-, and Fe-Salen COF, respectively (Table S3). In agreement with magnetic susceptibility and XPS observations, this modulation displays a pronounced metal-dependent trend, with a more substantial effect observed for metals possessing larger

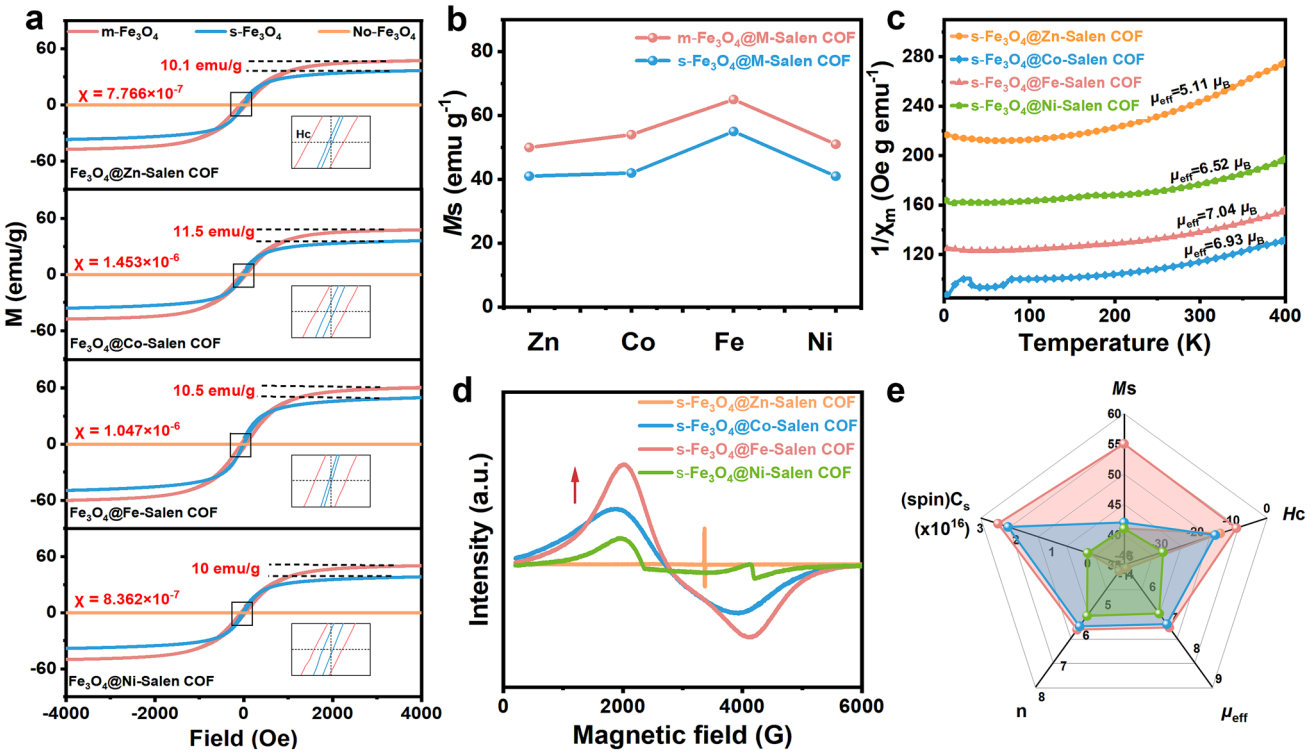

Fig. 2 Magnetic characterization of the composites. **a** Magnetic hysteresis loops and **b** the saturation magnetization (*Ms*) of catalysts at room temperature of MSA-Salen COFs and s/m-Fe_3O_4@MSA-Salen COFs. **c** ZFC curves related to the magnetic susceptibility of s-Fe_3O_4@MSA-Salen COFs. **d** EPR spectra of s-Fe_3O_4@MSA-Salen COFs. **e** Radar chart depicting magnetic characteristics of different metal materials

intrinsic magnetic moments (Fe, Co) (Fig. 2e). These characterized results demonstrate that the MMFR-C platform enables magnetic field-mediated spin polarization of active metal centers, establishing a direct correlation between microscopic electronic/spin states and macroscopic magnetic properties.

3.3 Electrochemical Performance of ORR

The ORR electrocatalytic activities of MSA-Salen COFs and the corresponding MMFR-C were evaluated using a standard three-electrode configuration in O_2-saturated 0.1 M KOH at room temperature. CV curve shows well-defined reduction peaks for MSA-Salen COFs and s-Fe_3O_4@MSA-Salen COFs in O_2-saturated electrolyte, with no obvious response in N_2-saturated solution, verifying their intrinsic ORR electrocatalytic activity (Fig. S15). As depicted in Fig. 3a, linear sweep voltammetry (LSV) demonstrates that s-Fe_3O_4@MSA-Salen COFs exhibit significantly enhanced ring current relative to pristine MSA-Salen COFs, underscoring the key role of magnetic Fe_3O_4 incorporation in regulating the ORR pathway and catalytic selectivity within the bioinspired MMFR-C platform.

RRDE measurements were employed to quantify H_2O_2 selectivity and electron transfer number, with a collection efficiency of 0.37 (Fig. S16). The electron transfer numbers for Zn-, Ni-, Co-, and Fe-Salen COF were determined to be 2.61, 2.53, 3.42, and 2.74, respectively, consistent with Koutecky–Levich (K–L) analysis (Figs. S17 and S18). The corresponding single-domain Fe_3O_4-integrated MMFR-C (s-Fe_3O_4@MSA-Salen COFs) exhibited n values of 2.60, 2.50, 2.75, and 2.47, accompanied by high H_2O_2 selectivity of 73.5, 72.8, 63.9, and 77.9%, respectively (Fig. 3a–c). These results unambiguously highlight the indispensable role of single-domain Fe_3O_4 in governing ORR pathway selectivity within the bioinspired MMFR-C by favoring the selective $2e^-$ ORR route. Notably, within the Co-Salen COF-derived MFR-C, the incorporation of single-domain Fe_3O_4 triggers a distinct catalytic pathway reversal from the intrinsic $4e^-$ process to the desired $2e^-$ route, achieving an over twofold enhancement in H_2O_2 selectivity.

https://doi.org/10.1007/s40820-026-02319-0

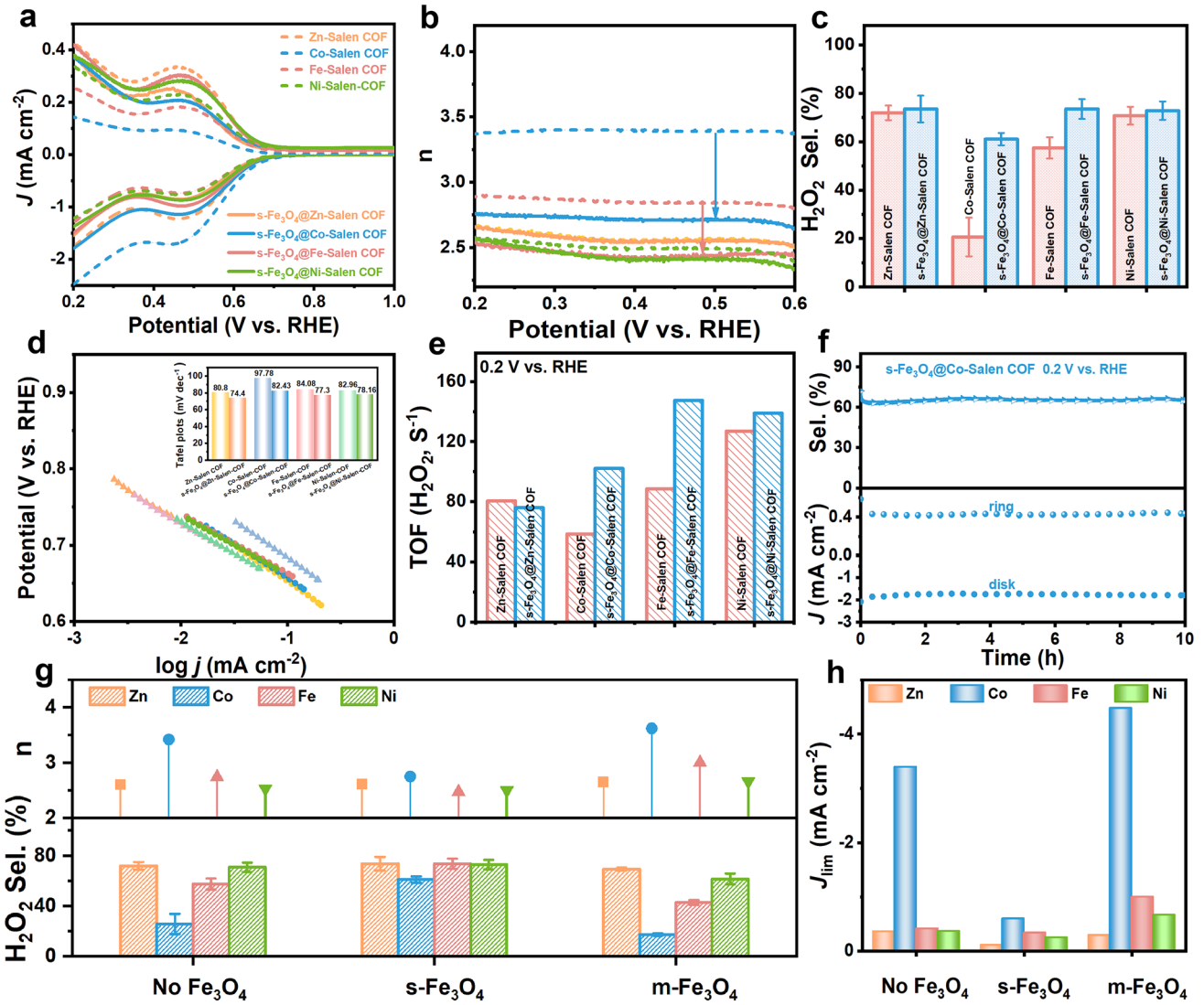

Fig. 3 **a** LSV curves of the synthesized catalysts at 1600 rpm, recorded at a scan rate of 10 mV s^{-1} in 0.1 M KOH. **b** Electron transfer number (n) and **c** H_2O_2 selectivity of the catalysts, derived from the LSV data. **d** Tafel plots and **e** TOF values at 0.2 V vs. RHE of MSA-Salen COF and s-Fe_3O_4@MSA-Salen COF. **f** Chronoamperometry measurement of s-Fe_3O_4@Co-Salen-COF for 36,000 s at 0.2 V vs. RHE. **g** Comparison chart of the n and H_2O_2 selectivity, and **h** limiting current diagram of H_2O_2RR for MSA-Salen COFs and s/m- Fe_3O_4@MSA-Salen COFs

Notably, the regulatory effect imposed by single-domain Fe_3O_4 is far more prominent in Co- and Fe-Salen COF-based systems than in Zn- and Ni-based counterparts. Such metal-dependent divergence originates from the stronger intrinsic magnetism and higher unpaired electron density in Co- and Fe-centered MMFR-C (Fig. 2e), which confer superior sensitivity to the built-in magnetic field derived from single-domain Fe_3O_4. This specific magnetic coupling within the bioinspired MMFR-C tailors the spin polarization of active metal sites, thereby fine-tuning the adsorption strength toward critical ORR intermediates and governing the overall pathway selectivity.

A lower Tafel slope is favorable for improving both the selectivity and efficiency of the $2e^-$ ORR pathway [40]. The Tafel slopes of s-Fe_3O_4@Zn-Salen COF, s-Fe_3O_4@Co-Salen COF, s-Fe_3O_4@Fe-Salen COF, and s-Fe_3O_4@Ni-Salen COF are 74.4, 82.43, 77.3, and 78.16 mV dec^{-1}, respectively, which are uniformly reduced compared with the pristine Zn-Salen COF (80.8 mV dec^{-1}), Co-Salen COF (97.78 mV dec^{-1}), Fe-Salen COF (84.08 mV dec^{-1}), and Ni-Salen COF (82.96 mV dec^{-1}) (Fig. 3d). This consistent reduction

directly demonstrates that single-domain Fe_3O_4 incorporation enhances the ORR electrocatalytic activity and accelerates reaction kinetics within the MMFR-C platform. Furthermore, the double-layer capacitance (C_{dl}) was evaluated through CV measurements within the non-Faradaic region at various scan rates (Fig. S19), which is directly proportional to electrochemically active surface area (ECSA). As shown in Fig. S20, MMFR-C composites (s-Fe_3O_4@MSA-Salen COFs) exhibit larger C_{dl} values than pristine MSA-Salen COFs, confirming that single-domain Fe_3O_4 in MMFR-C facilitates the exposure of more accessible active sites. Electrochemical impedance spectroscopy (EIS) measurements (Figs. S21 and S22) reveal that MMFR-C composites display smaller high-frequency semicircle radii than pristine COFs. This indicates that the synergistic interaction between single-domain Fe_3O_4 and metal single-atom COFs within MMFR-C effectively promotes charge transfer capability, further optimizing ORR performance.

To evaluate intrinsic catalytic activity, the H_2O_2-selective mass activity (MA(H_2O_2), Fig. S23) and turnover frequency (TOF) at 0.2 V vs. RHE (Fig. 3e) were analyzed. The single-domain Fe_3O_4-integrated MMFR-C (s-Fe_3O_4@MSA-Salen COFs) exhibited substantially superior MA(H_2O_2) and TOF compared to their pristine MSA-Salen COF counterparts, confirming that single-domain Fe_3O_4 within MMFR-C enhances intrinsic 2e$^-$ ORR activity. Notably, the Co-Salen COF-derived MMFR-C (s-Fe_3O_4@Co-Salen COF) achieved a remarkably high TOF of 102.14 s^{-1} and an MA(H_2O_2) of 93.61 mA mg^{-1} at 0.2 V vs. RHE, demonstrating exceptional 2e$^-$ ORR catalytic performance. Stability is a critical criterion for practical ORR applications [41]. Thus, the long-term stability of s-Fe_3O_4@Co-Salen COF was evaluated via chronoamperometry in O_2-saturated 0.1 M KOH at 0.2 V vs. RHE (Fig. 3f). Negligible decay in both disk and ring currents after 10 h of continuous operation confirmed the excellent long-term catalytic stability of this MMFR-C. We harvested s-Fe_3O_4@Co-Salen COF catalysts from the electrode surface and further carried out XRD and XPS characterizations. As revealed by XRD results (Fig. S24), the diffraction peak positions of the catalyst after stability cycling are highly consistent with those of the fresh sample, and no characteristic peaks corresponding to new phases are detected. This demonstrates that the intrinsic crystal structure of Fe_3O_4 and the skeleton structure of COF are well retained after long-term testing. Correspondingly, XPS analysis (Fig. S24b, c) further confirms that no obvious shifts occur in the binding energies and peak profiles of Co 2*p*, O 1 *s*, and N 1 *s* spectra after the stability test. In addition, cobalt species still predominantly maintain the + 2 oxidation state, which strongly evidences that the chemical valence state of active sites possesses excellent stability during prolonged electrocatalytic operation.

To investigate the effect of magnetic domains on ORR selectivity, the electrocatalytic performance of multi-domain Fe_3O_4-integrated MMFR-C (m-Fe_3O_4@MSA-Salen COFs) was evaluated. As shown in Fig. S25, the half-wave potentials of m-Fe_3O_4@Co-, Fe-, and Ni-Salen COFs all undergo a positive shift relative to their pristine MSA-Salen COF counterparts. RRDE measurements (Figs. 3g and S26) yield electron transfer numbers of 3.67, 3.02, and 2.66 for m-Fe_3O_4@Co-, Fe-, and Ni-Salen COFs, respectively, indicating a preference for the 4e$^-$ ORR pathway. These results confirm that multi-domain Fe_3O_4 acts as a key regulatory component within MMFR-C, facilitating the preferential occurrence of the 4e$^-$ ORR pathway.

To further clarify the role of s/m-Fe_3O_4 in MMFR-C, the intrinsic ORR performance of bare s/m-Fe_3O_4 particles was evaluated (Fig. S27). Bare Fe_3O_4 favors a near-3e$^-$ pathway, confirming that the tunable ORR selectivity of MMFR-C stems from the synergistic interaction between Fe_3O_4 and MSA-Salen COFs rather than the standalone catalytic activity of Fe_3O_4. Notably, RRDE measurements of s/m-Fe_3O_4 exhibit significant disk-ring current asymmetry, likely due to competitive side reactions causing a continuous increase in disk current. To gain additional insights into MMFR-C's ORR selectivity toward H_2O_2 production, polarization curves for the hydrogen peroxide reduction reaction (H_2O_2RR) were recorded in Ar-saturated 0.1 M KOH containing 50 mM H_2O_2 (Fig. S28), where current density comparison quantifies the capability to inhibit H_2O_2 decomposition. As depicted in Fig. 3h, single-domain Fe_3O_4-integrated MMFR-C (s-Fe_3O_4@MSA-Salen COFs) exhibits the lowest limiting current densities, endowing them with excellent ability to suppress H_2O_2 decomposition during the 2e$^-$ ORR process and thus favoring high-concentration H_2O_2 generation [42], which is consistent with the preceding RRDE results.

To optimize the loading amount, we systematically investigated Fe_3O_4 contents ranging from 10 to 30 wt%. XRD results showed that as the Fe_3O_4 content increased, the diffraction peak intensity of the COF gradually decreased (Fig. S29a, b). When the loading of multi-domain magnetite

https://doi.org/10.1007/s40820-026-02319-0

was further increased to 35 wt%, the crystallinity of the COF was significantly degraded; therefore, only the 10 – 30 wt% range was selected for electrochemical testing (Fig. S30). The test results indicated that the electron transfer number of the multi-domain material remained stable at approximately 3.67 within the 10 – 30 wt% range, while the single-domain material achieved the optimal regulation effect at 20 wt% (electron transfer number of 2.72). Considering these factors, 20 wt% was uniformly chosen as the representative loading. This content achieves saturated pathway regulation in each system while avoiding COF crystal quality degradation caused by excessively high loading.

The yield of H_2O_2 was quantitatively determined using the $K_2TiO(C_2O_4)_2$ colorimetric method (Figs. S31–S35) [43]. H_2O_2 yields at different constant currents showed that s-Fe_3O_4@Zn-Salen COF, s-Fe_3O_4@Co-Salen COF, s-Fe_3O_4@Fe-Salen COF, and s-Fe_3O_4@Ni-Salen COF achieved H_2O_2 production rates of 77.93, 93.35, 119.74, and 76.64 mmol g^{-1} h^{-1} at 0.2 V vs. RHE, with corresponding Faradaic efficiencies (FE) of 74.02, 61.27, 73.58, and 67.78%, respectively. It is indicated that the MMFR-C exhibits significantly enhanced H_2O_2 production rates and higher Faradaic efficiencies compared to their pristine MSA-Salen COF. This improvement is particularly pronounced for the Co- and Fe-based systems, indicating a marked enhancement in both selectivity and activity toward the two-electron oxygen reduction pathway for H_2O_2 generation. These findings are consistent with and corroborate the earlier LSV results. Notably, the s-Fe_3O_4@Fe-Salen COF composite achieves an H_2O_2 production rate as high as 132 mmol g^{-1} h^{-1} at 0.3 V vs. RHE. This enhancement is attributed to the moderate spin polarization effect induced by the magnetic s-Fe_3O_4 nanoparticles on the Fe-Salen COF, which promotes electron transfer and optimizes the adsorption of key reaction intermediates.

Meanwhile, to validate the above trends, the H_2O_2 production rate and FE of multi-domain Fe_3O_4-integrated MMFR-C (m-Fe_3O_4@Co/Fe/Ni-Salen COFs) were quantified at 0.3 V vs. RHE. As displayed in Fig. S36a–c, both H_2O_2 yield and FE decrease monotonically with increasing Fe_3O_4 domain size. This result further confirms that large multi-domain Fe_3O_4 within MMFR-C favors the competing 4e$^-$ ORR pathway at the expense of the 2e$^-$ route for H_2O_2 generation, which is fully consistent with the earlier LSV measurements.

Given the outstanding 2e$^-$ ORR performance and high H_2O_2 productivity of s-Fe_3O_4@Fe-Salen COF and s-Fe_3O_4@Co-Salen COF within the MMFR-C series, their potential for practical environmental remediation was further explored [44]. As H_2O_2 serves as a key oxidant for advanced oxidation processes, the in situ electrogenerated H_2O_2 was employed to degrade Rhodamine B as a model organic pollutant. H_2O_2 generated at 0.2 V vs. RHE over 3 h in an H-cell was collected for degradation tests. UV–Vis spectra and visual inspection confirmed complete degradation of the dye within 1 h (Fig. S37a, b), demonstrating efficient in situ H_2O_2 production by these MMFR-C.

3.4 Insight into the Catalytic Mechanism

In situ attenuated total reflectance Fourier-transform infrared spectroscopy (ATR-FTIR) spectra reveal that for single-domain MMFR-C (s-Fe_3O_4@Co-Salen COF), characteristic peaks at ~ 1250 and 872 cm^{-1}, consistent with *OOH stretching vibrations [45], are significantly intensified as the potential decreases (Figs. 4a and S38a). A weak H_2O_2 signal at 1407 cm^{-1} further confirms the dominance of the 2e$^-$ pathway. By contrast, multi-domain MMFR-C (m-Fe_3O_4@Co-Salen COF) shows markedly diminished *OOH signals, with new peaks at 1440 and 1086 cm^{-1} assignable to *O and *OH, typical of the 4e$^-$ pathway (Figs. 4b and S38b) [46]. Spin-polarized density functional theory (DFT) calculations were performed to elucidate the spin-dependent ORR kinetics over single-domain and multi-domain MMFR-C (Fig. S39). Gibbs free energy profiles identify *OOH formation as the rate-determining step for the 2e$^-$ pathway (Fig. 4c) [47]. Single-domain MMFR-C (s-Fe_3O_4@Co-Salen COF) delivers an ultralow-energy barrier of only 0.037 eV for *OOH generation, with *OOH stabilized at a higher free energy state to favor desorption as H_2O_2 instead of O–O cleavage. Multi-domain MMFR-C (m-Fe_3O_4@Co-Salen COF) presents a substantially higher barrier of 0.36 eV for the same step, while stabilizing *OOH at a lower free energy level to facilitate its dissociation into *O/*OH. These thermodynamic distinctions establish single-domain MMFR-C as a selective 2e$^-$ ORR catalyst and multi-domain MMFR-C as a preferential 4e$^-$ ORR catalyst with promoted O–O bond cleavage.

The projected density of states (PDOS) analysis of the Co 3*d* orbitals (Fig. S40) reveals that the m-Fe_3O_4@Co-Salen COF exhibits more pronounced asymmetry in the electron distribution across different *d*-orbitals, highlighting stronger

spin polarization features compared to the s-Fe_3O_4@Co-Salen COF, which shows relatively weaker spin polarization. This discrepancy arises from the distinct strengths of internal magnetic fields within the two MMFR-C variants, which induce varying degrees of polarization at the Co active sites.

Integrated experimental and theoretical results identify *OOH adsorption strength as a key descriptor for ORR selectivity, which is closely linked to the *d*-band center of the Co active site [48]. As shown in Fig. 4d, the calculated *d*-band center value for Co-Salen COF is –2.58. Single-domain MMFR-C (s-Fe_3O_4@Co-Salen COF) slightly downshifts the *d*-band center to − 2.67 eV, weakening the CO–OOH interaction to an optimal strength. This favors *OOH formation and protonation while suppressing O–O cleavage, directing the reaction to the $2e^-$ pathway for H_2O_2 production. Multi-domain MMFR-C upshifts the *d*-band center to − 2.26 eV via stronger spin polarization, strengthening *OOH adsorption, and promoting O–O bond cleavage to drive the $4e^-$ route. These trends are fully supported by free energy barriers, in situ ATR-FTIR, and electrochemical performance. These results demonstrate that the magnetic domain in MMFR-C enables precise tuning of the spin polarization and *d*-band center, allowing selective and controllable switching between $2e^-$ and $4e^-$ ORR pathways by optimizing *OOH adsorption energy (Fig. 4e).

Magnetic catalysts can effectively overcome spin-forbidden O_2 activation via spin-polarized charge transfer, lowering the kinetic barrier for the initial reaction step [49]. Given side-on O_2 adsorption at the Co single-atom site, M − O bond formation relies on hybridization between O_2 π* orbitals and dz^2 and *dxz-dyz* orbitals, whose extent directly governs $*O_2$ activation (Fig. 4f and Table S4). Single-domain MMFR-C (s-Fe_3O_4@Co-Salen COF) induces only a minor upshift of the Co dz^2 orbital (0.007 eV) and a downshift of the *dxz-dyz* orbitals (0.326 eV). Moderate spin polarization enables initial O_2 activation while suppressing electron backdonation to O_2 π* orbitals, stabilizing *OOH and inhibiting O–O cleavage to favor the $2e^-$ pathway [24]. Multi-domain MMFR-C (m-Fe_3O_4@Co-Salen COF) delivers a pronounced upshift of the Co dz^2 orbital (0.228 eV), strengthening orbital hybridization and improving spin matching between Co-3*d* and O-2*p*. This facilitates efficient overcoming of the spin prohibition during O_2 activation, paving the way for subsequent O–O bond cleavage and thus the $4e^-$ pathway. DFT calculations reveal the charge transfer between *OOH and the Co active site. DFT analysis further shows that single-domain MMFR-C exhibits a smaller Bader charge (1.25 e^-) than multi-domain MMFR-C (1.26 e^-), weakening Co–*OOH binding and promoting *OOH desorption for selective H_2O_2 generation.

PDOS calculations were performed for s-Fe_3O_4@Co-Salen COF and m-Fe_3O_4@Co-Salen COF following *OOH adsorption. Hybridization between the Co *d*-band and O *p*-band emerges upon oxygen adsorption, and the energy gap between their band centers reflects the metal-intermediate interaction strength. The gap is determined to be 4.60 eV for single-domain MMFR-C and 4.64 eV for multi-domain MMFR-C (Fig. 4g) [50]. The narrower gap in single-domain MMFR-C indicates a moderate Co–*OOH binding strength, which is optimal for H_2O_2 generation.

As shown in Fig. 4h, single-domain MMFR-C forms the Co− *OOH bond primarily via the *dyz* orbital, which is energetically downshifted relative to the Fermi level (E_f) [51]. This, along with a lower *d*-band center of –2.03 eV (Fig. S41), indicates moderate *OOH adsorption, facilitating *OOH hydrogenation and H_2O_2 desorption to favor the $2e^-$ pathway. Multi-domain MMFR-C is dominated by the *dyz* orbital near E_f, with a higher *d*-band center of − 1.64 eV that strengthens *OOH adsorption. This stabilizes *OOH and reduces the O–O bond cleavage barrier, driving the formation of *O/*OH intermediates and directing the ORR to the $4e^-$ route.

Figure 4i illustrates the complete catalytic cycles for the $2e^-$ and $4e^-$ ORR pathways over the MMFR-C. The reaction commences with spontaneous adsorption of ground-state O_2 at the coordinatively unsaturated metal active center, followed by proton-coupled electron transfer to generate the *OOH intermediate, which is the key branching point determining ORR selectivity. In single-domain MMFR-C, moderate, uniform spin polarization from the internal magnetic field modulates the metal site's electronic structure and orbital hybridization, optimizing *OOH adsorption energy to a thermodynamically favorable range. This moderate binding stabilizes the metal–OOH adduct, enabling preferential protonation of the proximal oxygen coordinated to the metal center. This promotes H_2O_2 reductive elimination and

https://doi.org/10.1007/s40820-026-02319-0

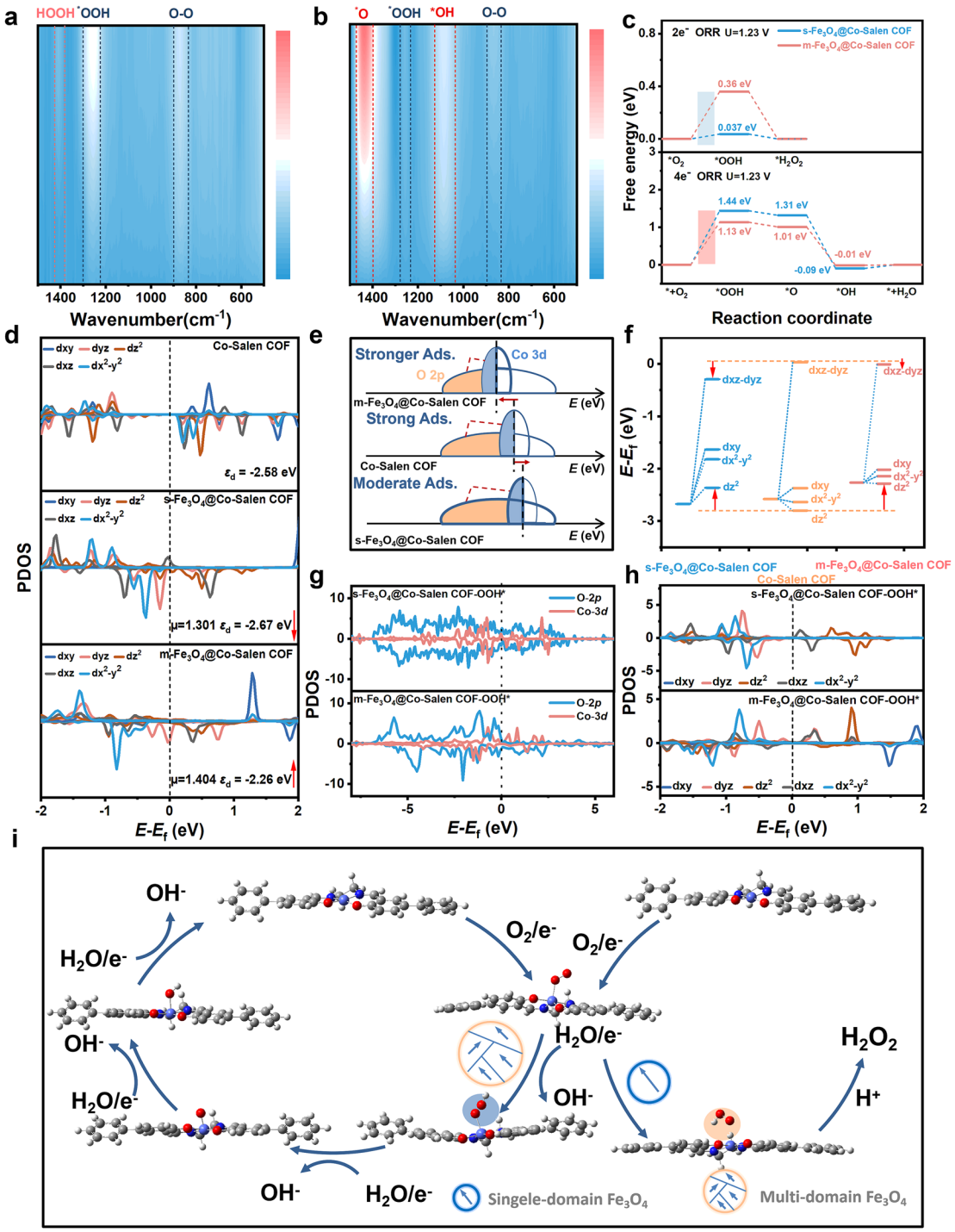

Fig. 4 In situ ATR-FTIR spectra of **a** s-Fe_3O_4@Co-Salen-COF and **b** m-Fe_3O_4@Co-Salen-COF catalysts in O_2-saturated 0.1 M KOH solution (pH 13) at different potentials from 0.8 to 0 V vs. RHE. **c** Free energy profiles for $2e^-$ ORR and $4e^-$ ORR of s-Fe_3O_4@Co-Salen-COF and m-Fe_3O_4@Co-Salen-COF. **d** Projected density of states (PDOS) of Co-Salen-COF, s-Fe_3O_4@Co-Salen-COF and m-Fe_3O_4@Co-Salen-COF. **e** Energy band structure diagrams. **f** Band energy structures of Co-Salen-COF, s-Fe_3O_4@Co-Salen-COF, and m-Fe_3O_4@Co-Salen-COF. **g** PDOS of the Co center and the O atom in OOH* intermediate for s-Fe_3O_4@Co-Salen-COF and m-Fe_3O_4@Co-Salen-COF. **h** Computed PDOS of s-Fe_3O_4@Co-Salen-COF and m-Fe_3O_4@Co-Salen-COF after OOH* adsorption. **i** Schematic ORR process on the N_2–M–O_2 site of MSA-Salen-COF

metal site regeneration, selectively channeling the reaction toward the $2e^-$ pathway for high-yield H_2O_2 production. In multi-domain MMFR-C, stronger, localized magnetic ordering induces intensive spin polarization at the metal site, significantly strengthening the metal–*OOH interaction. Enhanced orbital overlap and charge transfer favor protonation of the distal oxygen in metal–OOH, triggering O–O bond cleavage to form a metal-bound *O intermediate and free H_2O. Subsequent proton-coupled electron transfer steps drive the reaction toward the complete $4e^-$ pathway for H_2O formation.

4 Conclusions

In summary, this work establishes a novel strategy by constructing bioinspired MMFR-C to realize on-demand, reversible switching between the $2e^-$ and $4e^-$ ORR pathways. A mild, uniform endogenous magnetic field from single-domain MMFR-C optimizes orbital hybridization and *OOH adsorption energy, suppressing O–O bond cleavage to favor H_2O_2 generation. Representative single-domain MMFR-C (s-Fe_3O_4@Co-Salen COF) achieves 63.9% H_2O_2 selectivity with an electron transfer number of 2.72, far exceeding pristine Co-Salen COF (26% selectivity, $n = 3.48$). By contrast, a stronger magnetic field in multi-domain MMFR-C (m-Fe_3O_4@Co-Salen COF) optimizes the *d*-band center, lowers spin transition barriers, and enhances intermediate adsorption, promoting O–O bond cleavage and directing the ORR to the $4e^-$ pathway ($n = 3.67$). This work demonstrates that MMFR-C enables precise on-demand ORR pathway control, providing a new paradigm for designing selectivity-tunable ORR electrocatalysts.

Acknowledgements This work was financially supported by the National Natural Science Foundation of China (Grant Nos. 22375056, 22105058, and 22409050), Key Technology Research and Development Major Program of Hebei Province, China (Grant No. 242G4403Z), Central Government Guiding Fund for Local Science and Technology Development Program (Hebei, Grant No. 254Z4901G), Natural Science Foundation of Hebei Province (Grant Nos. B2024208065 and B2025208105), and Hebei Provincial Higher Education Institutions Scientific Research Project (Grant Nos. JCZX2026015 and JCZX2026039).

Author Contributions B. Z. and Q. G helped in experiments, data curation, and original draft—writing, DFT helped in theoretical calculation and conceptualization. H. L. helped in investigation, methodology, and data curation. Y. W. and Q. L. worked in supervision. H. L. and S. Q. helped in conceptualization, project administration, writing—review and editing, and funding acquisition.

Declarations

Conflict of interest The authors declare no conflict of interest. They have no known competing financial interests or personal relationships that could have appeared to influence the work reported in this paper.

Supplementary Information The online version contains supplementary material available at https://doi.org/10.1007/s40820-026-02319-0.

References

1. K. Chen, J. Huang, J. Chen, J. Gao, Z. Lu et al., Neighboring iron single atomic sites boost PtCo intermetallic activity for high-durability ORR electrocatalysis. Energy Environ. Sci. **18**(13), 6732–6743 (2025). https://doi.org/10.1039/d5ee00624d
2. Y. Zeng, X. Wang, W. Qi, C. Liu, L. Lu et al., Aligned d-orbital energy level of dual-atom sites catalysts for oxygen reduction reaction in anion exchange membrane fuel cells. Nat. Commun. **16**, 8111 (2025). https://doi.org/10.1038/s41467-025-63322-4
3. Z. Liang, H. Lei, H. Zheng, H.-Y. Wang, W. Zhang et al., Selective two-electron and four-electron oxygen reduction reactions using co-based electrocatalysts. Chem. Soc. Rev. **54**(11), 5248–5291 (2025). https://doi.org/10.1039/d4cs01199f
4. Y. He, S. Huang, X. Li, Y. Huang, D. Cao et al., Molecular engineering of covalent organic frameworks for electrocatalytic oxygen reduction reaction. Coord. Chem. Rev. **544**, 216972 (2025). https://doi.org/10.1016/j.ccr.2025.216972
5. A. Zadehnazari, F. Auras, D. Koumoulis, A. Abbaspourrad, Charge transfer in triphenylamine–tetrazine covalent organic frameworks for solar-driven hydrogen peroxide production. Nat. Commun. **17**, 72 (2026). https://doi.org/10.1038/s41467-025-66679-8

6. A. Yu, Y. Yang, Atomically dispersed metal catalysts for oxygen reduction reaction: two-electron *vs*. four-electron pathways. Angew. Chem. Int. Ed. **64**(16), e202424161 (2025). https://doi.org/10.1002/anie.202424161
7. J. Sun, M. Shen, A. Chang, J. Huang, P. Wang et al., Asymmetric Fe-N_3Se single atoms coupled with Fe atomic clusters on alveolar-inspired hierarchically porous carbon submicronspheres for enhanced oxygen reduction. Appl. Catal. B Environ. Energy **383**, 126102 (2026). https://doi.org/10.1016/j.apcatb.2025.126102
8. C. Yang, F. Sun, Y. Zhang, Z. Qu, J. Zuo et al., Unveiling the coupling effect of sp^2 domain size and local active sites in switching the selectivity of nanocarbon catalysts toward the oxygen electro-reduction. Nat. Commun. **16**(1), 11270 (2025). https://doi.org/10.1038/s41467-025-66161-5
9. Y. Wang, G.I.N. Waterhouse, L. Shang, T. Zhang, Electrocatalytic oxygen reduction to hydrogen peroxide: from homogeneous to heterogeneous electrocatalysis. Adv. Energy Mater. **11**(15), 2003323 (2021). https://doi.org/10.1002/aenm.202003323
10. Y. Fu, Q. Zhao, Q. Wei, C.R. Bowen, W.-Y. Wong et al., Non-precious metal-based single-atom catalysts for oxygen reduction reaction: fundamentals and applications. Mater. Sci. Eng. R. Rep. **160**, 100822 (2024). https://doi.org/10.1016/j.mser.2024.100822
11. X. Yan, X. Yuan, L. Ning, L. Bin, Z. Liang et al., Spatial engineering and d-orbital coupling in axial dual-atom sites for bifunctional oxygen catalysis. Nat. Commun. **16**, 11376 (2025). https://doi.org/10.1038/s41467-025-66362-y
12. M. Yang, W. Song, C. Chen, X. Yang, Z. Zhuang et al., Atomically dispersed Co/Mo sites anchored on mesoporous carbon hollow spheres for highly selective oxygen reduction to hydrogen peroxide in acidic media. Adv. Mater. **37**(17), 2416401 (2025). https://doi.org/10.1002/adma.202416401
13. Y. Zhao, J. Wan, C. Ling, Y. Wang, H. He et al., Acidic oxygen reduction by single-atom Fe catalysts on curved supports. Nature **644**(8077), 668–675 (2025). https://doi.org/10.1038/s41586-025-09364-6
14. Y. Shi, L.-L. Zhang, C. Wang, S. Sun, Heterostructure of Fe_3O_4 confined in hierarchical porous carbon for interface-enhanced medical-grade H_2O_2 electrosynthesis. Adv. Sci. **12**(27), 2502388 (2025). https://doi.org/10.1002/advs.202502388
15. X. Dong, S. Tao, G. Wang, J. Chen, R. Wang et al., Microenvironment regulation of asymmetric Fe coordination centers through designing p-n junction toward highly efficient oxygen reduction for rechargeable zinc-air batteries. Nano Energy **134**, 110553 (2025). https://doi.org/10.1016/j.nanoen.2024.110553
16. P. Shao, Z. Ren, B. Zhao, X. Wang, J. Li et al., Theory-guided design of N-confused porphyrinic covalent organic frameworks for oxygen reduction reaction. J. Am. Chem. Soc. **147**(10), 8769–8777 (2025). https://doi.org/10.1021/jacs.4c18645
17. X. Mei, X. Zhao, H. Du, B. Deng, H. Zhuo et al., Adjusting the active site of single Co atoms on CeO_2 *via* cyano functional groups for selective H_2O_2 electrosynthesis at high yield. Appl. Catal. B Environ. Energy **374**, 125398 (2025). https://doi.org/10.1016/j.apcatb.2025.125398
18. K.-M. Zhao, D.-X. Wu, W.-K. Wu, J.-B. Nie, F.-S. Geng et al., Identifying high-spin hydroxyl-coordinated $Fe^{3+}N_4$ as the active centre for acidic oxygen reduction using molecular model catalysts. Nat. Catal. **8**(5), 422–435 (2025). https://doi.org/10.1038/s41929-025-01324-7
19. W. Fang, K. Xu, X. Wang, Y. Zhu, X. Li et al., Heteroatom-coordinated Fe-N_4 catalysts for enhanced oxygen reduction in alkaline seawater zinc-air batteries. Nano-Micro Lett. **18**(1), 96 (2026). https://doi.org/10.1007/s40820-025-01943-6
20. P. Vensaus, Y. Liang, J.P. Ansermet, G.J.A.A. Soler-Illia, M. Lingenfelder, Enhancement of electrocatalysis through magnetic field effects on mass transport. Nat. Commun. **15**(1), 2867 (2024). https://doi.org/10.1038/s41467-024-46980-8
21. Y. Wang, P. Meng, Z. Yang, M. Jiang, J. Yang et al., Regulation of atomic Fe-spin state by crystal field and magnetic field for enhanced oxygen electrocatalysis in rechargeable zinc-air batteries. Angew. Chem. Int. Ed. **62**(28), e202304229 (2023). https://doi.org/10.1002/anie.202304229
22. J. Song, D. He et al., Magnetic field-enhanced acidic CO_2 electroreduction reaction on single nickel-site catalysts. J. Am. Chem. Soc. **147**(19), 16198–16206 (2025). https://doi.org/10.1021/jacs.5c00858
23. B. Jing, Q. Zhang, M. Liu, S. Yang, J. Zhang et al., Magnetically-altered eg-orbital occupancy to boost the two-electron oxygen reduction electrocatalysis for faster water decontamination. Appl. Catal. B Environ. Energy **369**, 125149 (2025). https://doi.org/10.1016/j.apcatb.2025.125149
24. Z. Yu, D. Zhang, Y. Wang, F. Liu, F. She et al., Spin manipulation of heterogeneous molecular electrocatalysts by an integrated magnetic field for efficient oxygen redox reactions. Adv. Mater. **36**(45), 2470360 (2024). https://doi.org/10.1002/adma.202470360
25. M. Wikström, K. Krab, V. Sharma, Oxygen activation and energy conservation by cytochrome c oxidase. Chem. Rev. **118**(5), 2469–2490 (2018). https://doi.org/10.1021/acs.chemrev.7b00664
26. D. Kass, S. Katz, H. Özgen, S. Mebs, M. Haumann et al., A bioinspired nonheme Fe^{III}–(O_2^{2-})–Cu^{II} complex with an S_t = 1 ground state. J. Am. Chem. Soc. **146**(36), 24808–24817 (2024). https://doi.org/10.1021/jacs.4c04492
27. T. Xie, Y. Wang, Y. Yue, S. Shen, Y. Xiong, Design of covalent organic frameworks mimicking cytochrome c oxidase for enhanced electrocatalytic oxygen reduction. Adv. Funct. Mater. **36**(22), e22948 (2026). https://doi.org/10.1002/adfm.202522948
28. I. Ishigami, R.G. Sierra, Z. Su, A. Peck, C. Wang et al., Structural insights into functional properties of the oxidized form of cytochrome c oxidase. Nat. Commun. **14**(1), 5752 (2023). https://doi.org/10.1038/s41467-023-41533-x
29. B. Zhang, L. Chen, Z. Zhang, Q. Li, P. Khangale et al., Modulating the band structure of metal coordinated salen COFs and an *in situ* constructed charge transfer heterostructure for

electrocatalysis hydrogen evolution. Adv. Sci. **9**(22), 2105912 (2022). https://doi.org/10.1002/advs.202105912

30. W. Zhou, X. Wang, W. Zhao, N. Lu, D. Cong et al., Photocatalytic CO_2 reduction to syngas using metallosalen covalent organic frameworks. Nat. Commun. **14**, 6971 (2023). https://doi.org/10.1038/s41467-023-42757-7
31. M. Liu, J. Zhang, H. Su, Y. Jiang, W. Zhou et al., *In situ* modulating coordination fields of single-atom cobalt catalyst for enhanced oxygen reduction reaction. Nat. Commun. **15**, 1675 (2024). https://doi.org/10.1038/s41467-024-45990-w
32. H. Dong, L. Fang, K.-X. Chen, J.-X. Wei, J.-X. Li et al., Dual metallosalen-based covalent organic frameworks for artificial photosynthetic diluted CO_2 reduction. Angew. Chem. Int. Ed. **64**(2), e202414287 (2025). https://doi.org/10.1002/anie.202414287
33. Y. Wada, T. Maruchi, R. Ishii, Y. Sunada, Visible light responsive dinuclear zinc complex consisting of proximally arranged two d10-zinc centers. Angew. Chem. Int. Ed. **62**(50), e202310571 (2023). https://doi.org/10.1002/anie.202310571
34. X. Ren, T. Wu, Y. Sun, Y. Li, G. Xian et al., Spin-polarized oxygen evolution reaction under magnetic field. Nat. Commun. **12**(1), 2608 (2021). https://doi.org/10.1038/s41467-021-22865-y
35. J. Ge, R.R. Chen, X. Ren, J. Liu, S.J.H. Ong et al., Ferromagnetic–antiferromagnetic coupling core–shell nanoparticles with spin conservation for water oxidation. Adv. Mater. **33**(42), 2101091 (2021). https://doi.org/10.1002/adma.202101091
36. L. Wang, J. Bao, L. Wang, F. Zhang, Y. Li, One-pot synthesis and bioapplication of amine-functionalized magnetite nanoparticles and hollow nanospheres. Chem **12**(24), 6341–6347 (2006). https://doi.org/10.1002/chem.200501334
37. Z.-Y. Mei, G. Zhao, C. Xia, S. Cai, Q. Jing et al., Regulated high-spin state and constrained charge behavior of active cobalt sites in covalent organic frameworks for promoting electrocatalytic oxygen reduction. Angew. Chem. Int. Ed. **62**(27), e202303871 (2023). https://doi.org/10.1002/anie.202303871
38. H. Zhang, H.-C. Chen, S. Feizpoor, L. Li, X. Zhang et al., Tailoring oxygen reduction reaction kinetics of Fe−N−C catalyst *via* spin manipulation for efficient zinc–air batteries. Adv. Mater. **36**(25), 2400523 (2024). https://doi.org/10.1002/adma.202400523
39. C. Wang, Y. Yang, J. Zheng, Y. Yuan, D. Pang et al., Magnetic field-driven spin state transformation in promoting the catalytic activity of doped single-atom for hydrogen evolution reaction. Adv. Mater. **38**(6), e13213 (2026). https://doi.org/10.1002/adma.202513213
40. Y. Zou, Y. Zhang, C. Zhang, T. Bao, Y. Xi et al., Hydrogen-bonded organic framework@conductive metal-organic framework heterostructures for ampere-level hydrogen peroxide production. Nat. Commun. **16**, 10908 (2025). https://doi.org/10.1038/s41467-025-65887-6
41. Y. Liu, S. Liu, J. Jiang, X. Wei, K. Zhao et al., Monomolecule coupled to oxygen-doped carbon for efficient electrocatalytic hydrogen peroxide production. Adv. Mater. **37**(14), 2502197 (2025). https://doi.org/10.1002/adma.202502197
42. Q. Zhi, R. Jiang, X. Yang, Y. Jin, D. Qi et al., Dithiine-linked metalphthalocyanine framework with undulated layers for highly efficient and stable H_2O_2 electroproduction. Nat. Commun. **15**(1), 678 (2024). https://doi.org/10.1038/s41467-024-44899-8
43. Z. Bao, J. Zhao, S. Zhang, L. Ding, X. Peng et al., Synergistic effect of doped nitrogen and oxygen-containing functional groups on electrochemical synthesis of hydrogen peroxide. J. Mater. Chem. A **10**(9), 4749–4757 (2022). https://doi.org/10.1039/d1ta09915a
44. C. Yang, S. Shang, L. Lin, P. Wang, Z. Ye et al., Electro-driven cycling Fenton catalysis through two-dimensional electroresponsive metal–organic frameworks for water purification. Nat. Water **2**(8), 793–802 (2024). https://doi.org/10.1038/s44221-024-00262-1
45. H. Wu, L. Li, H. Chen, Y. Xing, Z. Wang et al., Topology control of covalent organic frameworks with interlaced unsaturated 2D and saturated 3D units for boosting electrocatalytic hydrogen peroxide production. Angew. Chem. Int. Ed. **63**(40), e202410719 (2024). https://doi.org/10.1002/anie.202410719
46. T. Xu, H. Zhou, X. Zhang, T.S. Herng, J. Ding et al., Covalent organic frameworks with carbon-centered radical sites for promoting the 4e− oxygen reduction reaction. Angew. Chem. Int. Ed. **64**(13), e202424449 (2025). https://doi.org/10.1002/anie.202424449
47. C. Xing, Y. Zou, L. Liu, D. Chu, D. Sun et al., Tuning Ni–O orbital interactions to steer oxygen activation for enhanced hydrogen peroxide photosynthesis. Sci. Bull. **71**(3), 587–597 (2026). https://doi.org/10.1016/j.scib.2025.12.053
48. P. Xia, T. He, T. Xu, Z.-S. Zhu, Y. Sun et al., Unlocking flooded domains in air-breathing cathodes with edge-located asymmetric CoN_2O_2 sites for robust H_2O_2 electrosynthesis. Appl. Catal. B Environ. Energy **383**, 126099 (2026). https://doi.org/10.1016/j.apcatb.2025.126099
49. M. Sun, J. Chen, Z. Zhang, Y. Jing, M. Zhao et al., Ferromagnetic ordering outperforms coordination effects in governing oxygen reduction catalysis on high-index nickel single crystals. Angew. Chem. Int. Ed. **64**(31), e202504869 (2025). https://doi.org/10.1002/anie.202504869
50. Q. An, X. Qin, X. Li, T. Yao, J. Guo et al., Hydrogen peroxide electrosynthesis under weak thermodynamic driving conditions enabled by *in situ* spin-state tailoring. Adv. Funct. Mater. **36**(31), e27886 (2026). https://doi.org/10.1002/adfm.202527886
51. L. Chen, X. Wang, T. Lu, H. Pang, S. Zhang et al., Maneuver of the d-orbital spin polarization of Fe single atomic sites *via* a near-range axial ligand effect for boosting oxygen reduction reaction. Appl. Catal. B Environ. Energy **366**, 125007 (2025). https://doi.org/10.1016/j.apcatb.2024.125007

 https://doi.org/10.1007/s40820-026-02319-0